Earth and Planetary Science Letters 578 (2022) 117317

Contents lists available at ScienceDirect

Earth and Planetary Science Letters

www.elsevier.com/locate/epsl

Diffusion anisotropy of Ti in zircon and implications for Ti-in-zircon thermometry

E.M. Bloch [a,*], M.C. Jollands [a,b], P. Tollan [c], F. Plane [a], A.-S. Bouvier [a], R. Hervig [d], A.J. Berry [e], C. Zaubitzer [f], S. Escrig [a,g], O. Müntener [a], M. Ibañez-Mejia [h], J. Alleon [a], A. Meibom [a,g], L.P. Baumgartner [a], J. Marin-Carbonne [a], M. Newville [i]

[a] Institute of Earth Sciences, Faculty of Geosciences and Environment, University of Lausanne, Lausanne CH-1015, Switzerland
[b] Lamont-Doherty Earth Observatory, Columbia University, Palisades, NY, 10964, USA
[c] Institute of Geochemistry and Petrology, ETH Zürich, Clausiusstrasse 25, Zürich CH-8092 Switzerland
[d] School of Earth and Space Exploration, Arizona State University, Tempe, AZ, 85281, USA
[e] Research School of Earth Sciences, Australian National University, Canberra, ACT 2601, Australia
[f] Scientific Center for Optical and Electron Microscopy (ScopeM), ETH Zürich, Zürich CH-8093 Switzerland
[g] Laboratory for Biological Geochemistry, School of Architecture, Civil and Environmental Engineering, Ecole Polytechnique Fédérale de Lausanne, Lausanne CH-1015, Switzerland
[h] Department of Geosciences, University of Arizona, Tucson, AZ, 85721, USA
[i] Center for Advanced Radiation Sources, University of Chicago, Chicago, IL, 60637, USA

ARTICLE INFO

Article history:
Received 10 May 2021
Received in revised form 11 November 2021
Accepted 21 November 2021
Available online xxxx
Editor: R. Dasgupta

Keywords:
Ti-in-zircon
thermometry
zircon
diffusion
diffusion anisotropy

ABSTRACT

Ti-in-zircon thermometry has become a widely used tool to determine zircon crystallization temperatures, in part due to reports of extremely sluggish Ti diffusion perpendicular to the crystallographic c-axis in this mineral. We have conducted Ti-in-zircon diffusion experiments, focusing on diffusion parallel to the c-axis, at 1 atm pressure between 1100 and 1540 °C, with oxygen fugacities equivalent to air and the Ni-NiO buffer. There is no resolvable dependence of Ti diffusion in zircon upon silica or zirconia activity, or upon oxygen fugacity. The diffusion coefficient of Ti in zircon is found to be a weak function of its own concentration, spanning less than 0.5 log units across any profile induced below 1300 °C. Ti diffusion in zircon, parallel to the c-axis at 1 atm pressure, is well described using:

$$\log_{10} D_{Ti} = \left[1.34(\pm 1.44) - \frac{555425(\pm 44820)\ \mathrm{J\,mol^{-1}}}{2.303\ \mathrm{RT\ (K)}}\right] \mathrm{m^2\,s^{-1}}$$

where R is the gas constant in J/(mol·K). In conjunction with diffusion coefficients for Ti in zircon perpendicular to the c-axis reported by Cherniak and Watson (2007), strong diffusion anisotropy for Ti in zircon is observed. Diffusion parallel to the c-axis is ~4-5 orders of magnitude faster than diffusion perpendicular to the c-axis within the experimentally constrained temperature range shared between these two studies (1540-1350 °C). This difference increases if the data are extrapolated to lower temperatures and reaches ~7.5-11 orders of magnitude between 950-600 °C, a typical range for zircon crystallization. Diffusion of Ti in natural zircons will predominantly occur parallel to the c-axis, and the Ti-in-zircon thermometer appears susceptible to diffusive modification under some crustal conditions. Temperatures calculated using this system should therefore be evaluated on a case-by-case basis, particularly when considering high-T, slowly cooled, reheated and/or small zircons.

* Corresponding author.
E-mail address: elias.bloch@unil.ch (E.M. Bloch).

https://doi.org/10.1016/j.epsl.2021.117317
0012-821X/

1. Introduction

Over the past several decades, zircon has emerged as one of the most useful minerals for the petrological, geochemical and geochronological study of igneous and metamorphic rocks. The chemical and isotopic compositions of zircon are routinely used to determine the physical conditions of zircon formation and to infer details of a wide range of geological processes (e.g., Grimes et al., 2015; Guo et al., 2020; Hoskin and Schaltegger, 2003; Ibañez-Mejia and Tissot, 2019; Rubatto, 2017; Wlde et al., 2001). The use of zircon has been bolstered by experimental studies that show diffusion of many important species (*e.g.*, Pb, REE, U, Th, Hf and Ti) to be exceptionally slow (Cherniak et al., 1997a,b; Cherniak and Watson, 2000, 2007; Suzuki et al., 1992). These data suggest that volume diffusion should play a negligible role in modifying the concentrations and/or isotopic compositions of these species under most crustal conditions.

The diffusion of tetravalent cations is particularly important in zircon, as the susceptibilities of these species to diffusive resetting have major implications for the interpretations of U-Pb geochronology (*e.g.*, Spencer et al., 2016), Zr and Hf isotopic compositions (e.g., Chen et al., 2020; Guo et al., 2020; Méheut et al., 2021; Tompkins et al., 2020) and temperatures retrieved from Ti-in-zircon thermometry (Ferry and Watson, 2007). Although experimental studies have reported extremely slow diffusion of tetravalent cations in zircon (Cherniak et al., 1997a; Cherniak and Watson, 2007; Suzuki et al., 1992), these studies only measured diffusion occurring perpendicular to the c-axis. Zircon is a tetragonal mineral and is therefore expected to exhibit some degree of diffusion anisotropy, with its two principal diffusion directions aligned parallel and perpendicular to the crystallographic c-axis (Nye, 1985). In this study we report the results of experiments on Ti-in-zircon diffusion from 1100-1540 °C at 1 atm pressure, in which we focus primarily on diffusion parallel to the c-axis.

2. Methods

2.1. Diffusion experiments

The diffusion experiments were conducted using ~3 × 3 × 3 mm cubes of oriented zircon, cut from two different stocks of natural crystals. The majority of the experiments used gem-quality zircon megacrysts originating from the central highlands of Vietnam (Huong et al., 2016; Sinh et al., 2019). These zircons (VZ zircons) contain sparse populations of apatite, hematite and ilmenite inclusions, which were easily avoided when the samples were sectioned. Several experiments were performed using zircon megacrysts from Tanzania (TZ zircons). Although the mineral dealer did not know the exact origin of these samples, it is likely that they come from the Tanga province, south of Umba, since this region produces similar high-quality zircons. The Tanzania zircons contain no visible fractures or inclusions.

Prior to cutting, zircon megacrysts were oriented using the Empyrean single-crystal X-ray diffractometer housed in the Crystal Growth Facility at the École Polytechnique Fédérale de Lausanne (EPFL). All visible faces with sufficient surface area were indexed, allowing us to determine the orientation of each crystal accurately. Most samples were cut such that the eventual polished diffusion interface would be perpendicular to the c-axis. Two samples were oriented so the diffusion interface would instead be parallel to the c-axis.

The cut zircons were mounted in thermoplastic acrylic, and polished stepwise using progressively finer diamond paste, down to 0.5 µm abrasive. A final polishing step was performed using a colloidal silica solution. Following removal from the acrylic, the crystals were thoroughly cleaned via sonication in isopropanol followed by de-ionized water, and then pre-annealed at 1300 °C for ~48 h. The purpose of pre-annealing is to equilibrate the defect concentrations within the crystals at or close to the experimental conditions, and to heal any elusive fast-diffusion paths that could have been generated during polishing. Pre-annealing minerals such as zircon, which commonly have high U concentrations, also serves to heal any radiation damage that might be present in the crystal lattice. Raman spectra recorded from zircons before and after pre-annealing are shown in Supplementary Fig. S1. After pre-annealing, the samples were again cleaned via sonication in de-ionized water.

Experiments were executed using a variety of powder diffusant sources, which were designed to impose varying silica, zirconia and titania activities ($aSiO_2$, $aZrO_2$ and $aTiO_2$, respectively) throughout diffusion anneals. All of the powders reside within

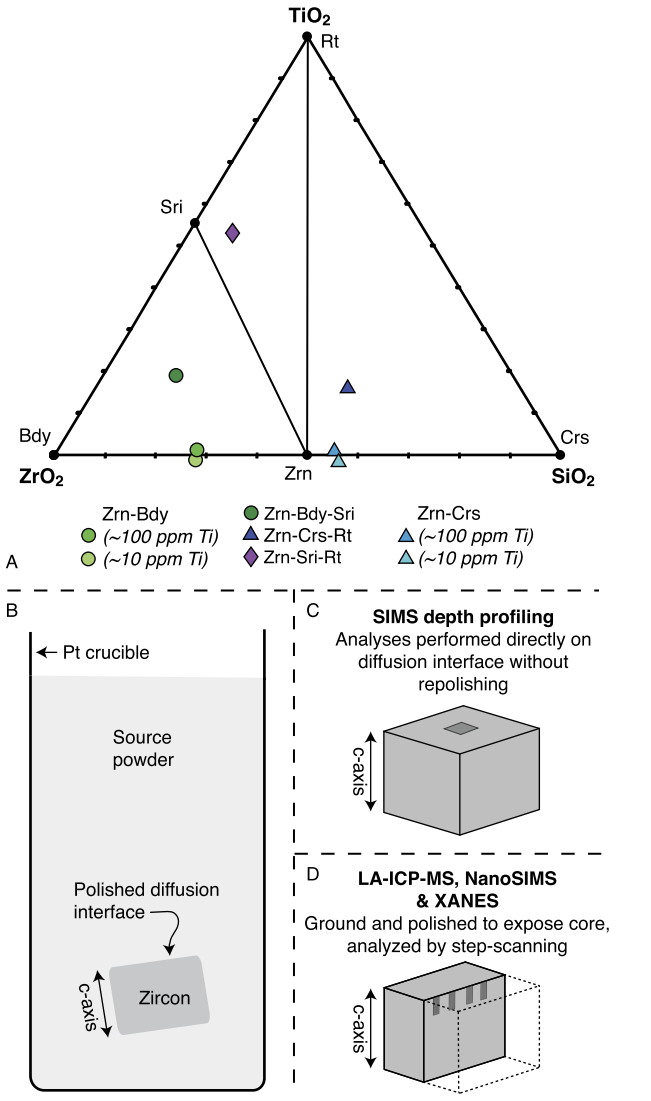

Fig. 1. Materials, experimental design and preparation for analyses. A: Composition of the buffering/Ti source powders. Phase diagram after Tailby et al. (2011). The vertical (TiO_2 dimension) placement of powders that do not contain a Ti-phase (srilankite or rutile) have been exaggerated to reduce overlap and add clarity. B: Experimental design. Oriented and polished zircons were packed into a Pt crucible where they were completely surrounded with source powder throughout the diffusion experiments. C: Preparation of zircons for SIMS depth-profiling analyses. D: Preparation of zircons for step-scanning analyses by LA-ICP-MS, NanoSIMS and XANES spectroscopy. See main text for further details. *Mineral abbreviations: Zrn = zircon, Sri = srilankite, Rt = rutile, Crs = cristobalite, Bdy = baddeleyite.* (For interpretation of the colors in the figure(s), the reader is referred to the web version of this article.)

Table 1
Summary of experimental conditions and retrieved diffusion coefficients of Ti in zircon parallel to the crystallographic c-axis. All experiments were conducted at 1 atm pressure. Diffusion profiles were measured by [a]SIMS depth profiling with the Cameca 1280HR at UNIL, [b]SIMS depth profiling with the Cameca 6f at ASU, [c]LA-ICP-MS, and [d]NanoSIMS. Values of $logD_{eff}$ ($logD_{max}$ - $\Delta logD/2$) were used to retrieve Arrhenius trends. See main text for details of uncertainty estimation. $\log fO_2 = -0.7$ corresponds to air. Mineral abbreviations: Zrn = zircon, Sri = srilankite, Rt = rutile, Crs = cristobalite, Bdy = baddeleyite.

Sample	Powder assemblage	$\log fO_2$	T (°C)	Time (s)	$logD_{max}$ (m^2/s)	±	$\Delta logD$ (m^2/s)	±	$logD_{eff}$ (m^2/s)	±
[c]VZ_ZTBSC3	Zrn-Bdy-Sri	−5.0	1500	1.889820×10^6	−14.54	0.12	0.89	0.16	−14.99	0.21
[c]VZ_ZTBSC4	Zrn-Bdy-Sri	−0.7	1450	4.414620×10^6	−15.16	0.12	0.53	0.20	−15.43	0.23
[c]VZ_ZTBSC10	Zrn-Bdy-Sri	−0.7	1400	1.451040×10^6	−15.74	0.14	0.75	0.12	−16.12	0.21
[a]VZ_ZTBSC7	Zrn-Bdy-Sri	−0.7	1300	3.020160×10^6	−17.03	0.15	.0.27	0.07	−17.17	0.18
[a]VZ_ZTBSC8	Zrn-Bdy-Sri	−0.7	1300	1.350000×10^6	−17.01	0.18	0.50	0.08	−17.26	0.23
[b]TZ_ZTBSC16	Zrn-Bdy-Sri	−0.7	1300	1.63380×10^5	−17.02	0.20	0.30	0.12	−17.17	0.27
[b]TZ_ZTBSC15	Zrn-Bdy-Sri	−0.7	1300	5.91600×10^5	−17.34	0.15	0.30	0.09	−17.49	0.21
[d]VZ_ZTBSC9	Zrn-Bdy-Sri	−0.7	1200	6.991740×10^6	−18.49	0.25	0.14	0.09	−18.56	0.30
[a,b]VZ_ZTBSC12	Zrn-Bdy-Sri	−0.7	1200	1.65600×10^5	−18.42	0.18	0.06	0.07	−18.45	0.22
[a]VZ_ZTBSC2	Zrn-Bdy-Sri	−0.7	1200	9.23400×10^5	−18.32	0.16	0.04	0.16	−18.34	0.25
[a]VZ_ZTBSC14	Zrn-Bdy-Sri	−0.7	1100	7.61460×10^5	−19.56	0.20	0.36	0.13	−19.74	0.29
[b]TZ_ZTBSC17	Zrn-Bdy-Sri	−0.7	1100	2.156280×10^6	−19.65	0.17	0.10	0.07	−19.70	0.21
[c]VZ_ZBC1	Zrn-Bdy (∼100 ppm Ti)	−0.7	1540	3.290040×10^6	−14.61	0.09	0.22	0.17	−14.72	0.19
[c]VZ_ZBC3	Zrn-Bdy (∼100 ppm Ti)	−5.0	1500	1.889820×10^6	−14.86	0.10	0.45	0.07	−15.09	0.14
[c]VZ_ZQRC3	Zrn-Crs-Rt	−5.0	1500	1.889820×10^6	−14.48	0.09	0.72	0.14	−14.84	0.18
[a]VZ_ZQRC7	Zrn-Crs-Rt	−0.7	1300	3.020160×10^6	−17.13	0.14	0.04	0.04	−17.15	0.17
[a,b]VZ_ZQRC14	Zrn-Crs-Rt	−0.7	1100	7.61460×10^5	−19.33	0.20	0.12	0.08	−19.39	0.24
[c]VZ_ZQC1	Zrn-Crs (∼100 ppm Ti)	−0.7	1540	3.290040×10^6	−14.41	0.13	0.31	0.10	−14.57	0.19
[d]VZ_ZSRC9	Zrn-Sri-Rt	−0.7	1200	6.991740×10^6	−18.37	0.22	0.48	0.16	−18.61	0.31
[c]VZ_ZBLC3	Zrn-Bdy (∼10 ppm Ti)	−5.0	1500	1.889820×10^6	−14.69	0.30	0.10	0.05	−14.74	0.33
[c]VZ_ZQLC3	Zrn-Crs (∼10 ppm Ti)	−5.0	1500	1.889820×10^6	−14.84	0.21	0.15	0.07	−14.92	0.25

the SiO_2-ZrO_2-TiO_2 ternary system (Fig. 1A), and were synthesized using a sol-gel approach modified after Karpe et al. (2014). Mixtures of zirconyl nitrate ($ZrO(NO_3)_2$) dissolved in dilute nitric acid, tetraethyl orthosilicate ($Si(OC_2H_5)_4$), titanium(IV) isopropoxide ($Ti[OCH(CH_3)_2]_4$) and ammonium titanyl oxalate monohydrate ($(NH_4)_2TiO(C_2O_4)_2{\cdot}H_2O$) dissolved in water (Supplementary Table S1) were combined in teflon beakers and then dried down on a magnetic hotplate while being stirred continuously with a teflon-coated magnet. Once the majority of the mixture had evaporated, a small amount of ammonium nitrate was added in order to promote rapid precipitation of nanocrystals from the solution. The dried products were then heated in a Pt crucible using a Bunsen burner to burn off the majority of residual N-H-C components. The remaining powders were ground using an agate mortar and pestle, packed into Pt crucibles and then annealed at 1300 °C in a box furnace for a minimum of 48 h. During this final annealing step, any remaining N-H-C components were removed from the mixtures, and the equilibrium phase assemblage (Table 1) formed. The final phase assemblages in each of these powders were verified by X-ray powder diffraction (Supplementary Fig. S2) using the ARL Thermo X'tra diffractometer housed in the Institute of Earth Sciences at the University of Lausanne.

Diffusion experiments were carried out at 1 atm pressure, in both Borel box furnaces and in a Gero vertical gas-mixing tube furnace in the hydrothermal experimental laboratory at the University of Lausanne. In both setups, temperature was monitored using a type-B thermocouple, yielding temperature uncertainties of 0.5%. Oriented and polished zircons were surrounded by source powder and packed into small Pt crucibles (Fig. 1B), so that multiple samples could be run simultaneously but still remain physically isolated. Experiments were run from 1100 – 1540 °C. The majority of diffusion experiments were done in air ($\log_{10} fO_2 = -0.7$), but several experiments at 1500 °C imposed an fO_2 equivalent to the Ni-NiO buffer ($\log_{10} fO_2 = -5.0$) by flowing a fixed ratio of CO_2-H_2 through the furnace tube. Experimental conditions are summarized in Table 1. After the experiments were completed, the powder source was easily removed and samples were cleaned by sonication in isopropanol and then in de-ionized H_2O. The high-quality polish of the diffusion interface was maintained in all experiments. Samples intended for secondary ion mass spectrometry (SIMS) depth profiling were not re-polished after diffusion anneals. Samples that were designated for laser-ablation inductively coupled plasma mass spectrometry (LA-ICP-MS) or NanoSIMS step scanning were ground halfway through the sample (perpendicular to the polished diffusion interface), mounted in epoxy and then re-polished using progressively finer diamond paste down to 1 µm abrasive (Fig. 1, panels C and D).

2.2. Analytical techniques

2.2.1. Secondary ion mass spectrometry (SIMS)

Depth profiling analyses were performed using both the Cameca 1280HR SIMS instrument housed in the SwissSIMS laboratory within the Center for Advanced Surface Analysis (CASA), and the Cameca ims 6f SIMS instrument in the School of Earth & Space Exploration at Arizona State University (ASU). Samples were mounted in indium prior to SIMS analysis, and a typical mount held 6-10 samples. All mounts were coated with ∼35 nm of Au, deposited by Au evaporation or sputter coating under vacuum, prior to analysis. On both SIMS machines, analyses included positive secondary ions of ^{28}Si and/or ^{30}Si, ^{49}Ti, ^{90}Zr and/or ^{96}Zr. The choice of which Si and Zr isotopes to measure depended on the machine settings in a given measurement, which themselves depended on the length of the diffusion profile being measured. Count times were 2 s for Si and Zr, and 10 s for Ti. In order to compensate for charging throughout the analyses, we applied an energy re-centering routine using ^{28}Si or ^{30}Si at the beginning of each cycle, starting at cycle 6. This routine varies the voltage at which the sample is held, such that the total counts of the given Si isotope are maximized.

On the 1280HR instrument at CASA, samples were held at +5 kV and sputtered with an $^{16}O_2^-$ primary ion beam (PIB), which was accelerated at −10 kV and generated using a Hyperion-II RF plasma source. The PIB was focused to a ∼10 µm spot and then rastered over a 125 × 125 µm area. A combination of electronic and field gating was used such that only secondary ions originating from the 20 x 20 µm region at the center of rastered area entered the mass spectrometer. Subsequent to depth profiling, the depth of each crater was measured using a Bruker ContourGT-K white-light microscope in order to assess the depth and topography of the resulting crater, with low topographical variation (< 20 nm) indicating uniform sampling depth throughout the depth profiling

measurements; data from craters that did not meet this criterion were disregarded.

On the 6f instrument at ASU, samples were also held at +5 kV and sputtered with a PIB of $^{16}O_2^-$, generated in a modified duoplasmatron held at −12.5 kV. The 30 to 50 nA PIB was focused to ∼30 um diameter and rastered over a 125 × 125 μm^2 area. The transfer lens settings were set for a ∼75 μm diameter maximum analyzed area, but a 100 μm diameter field aperture (field gating) was used to limit the ions detected to a ∼4 μm diameter circular area in the center of the sputtered crater, resulting in ∼20x lower ion intensity compared to the 1280 instrument. At these conditions, sputter rates were ∼0.2 to 0.3 nm/s. Secondary ions with 0 ± 20 eV initial kinetic energy were detected in electron multipliers. Crater depths were determined using an Alphastep 200 stylus profilometer, calibrated against step-height standards.

2.2.2. NanoSIMS

NanoSIMS analyses were performed using the Cameca 50L ion microprobe at the CASA facility in Lausanne. Areas of interest were sputtered with an $^{16}O^-$ PIB accelerated by 16 kV and focused to a spot size of ∼600 nm. Following an implantation phase required to reach a significant emission of secondary ions, 15 × 15 μm^2 images with 256 × 256 pixels resolution were rapidly collected using a dwell time of 2 ms per pixel. Based on the ion images obtained, the locations for line-scan profiles were defined perpendicular to the grain boundary. Line-scan profiles were acquired by repeatedly sputtering the target segment (25 scans) with a dwell time of 2s per pixel. For this study, ^{28}Si and ^{49}Ti ions were extracted and collected simultaneously by electron multipliers. The reported data correspond to the stacked values from all 25 scans.

2.2.3. Laser-ablation inductively coupled plasma mass spectrometry (LA-ICP-MS)

Two different LA-ICP-MS methods (scans and spots) were used, both employing the Thermo Scientific Element XR ICP-MS coupled with an Australian Scientific Instruments Resolution-LR laser ablation system, housed in the Institute of Geochemistry and Petrology at ETH Zürich. The majority of analyses utilized the scanning mode, whereby the stage was moved at a constant rate of 2 μm/s and the laser beam focused on-sample had dimensions of 6 × 100 μm, with the long axis parallel to the diffusion interface. The repetition rate of the laser was 10 Hz and the fluence maintained at around 4 J/cm^2. Ablation was conducted in a 2-volume cell, ensuring rapid washout of the ablated material. The aerosol was introduced to the ICP in a stream of He, Ar and N with flow rates of 500 ml/min, 1 l/min and 2 ml/min respectively. The isotopes measured were ^{29}Si (internal standard), ^{47}Ti, ^{49}Ti, ^{53}Cr, ^{89}Y, ^{91}Zr, ^{172}Yb and ^{178}Hf, with a total sweep time of ∼2 s. Approximately 30 s of gas blank was measured before each sample or standard ablation to determine the background counts. A cleaning run was conducted before each measurement to remove any surface contamination. The primary calibration standard, NIST 610, was measured at regular intervals along with secondary zircon standards 91500 and GZ7.

Several samples were also analyzed by performing transects in spot mode, both to measure Ti diffusion profiles and to characterize the trace element composition of the starting materials. The spot diameter was 19 μm, repetition rate was 4 Hz and fluence was 2.5 J/cm^2. Ablation persisted for 30 s and was conducted immediately following 30 s of background measurement. Gas flow rates and standards were the same as described above. An extended element list of the most commonly occurring lithophile trace elements was measured (Table 2) with a total scan time of approximately 0.6 s. All LA-ICP-MS datasets were reduced using Iolite 4 (Paton et al., 2011), employing a step forward function for the background and a polynomial function for the primary standard.

Table 2
Trace element compositions of starting materials. Trace element concentrations of the zircons used in diffusion experiments were measured via LA-ICP-MS in spot mode (see main text for details). All values are in ppm. Reported standard errors (s.e.) for the VZ and TZ zircons are based on 26 and 19 analyses, respectively. b.d. = below detection.

Element	VZ (ppm)	s.e. (VZ)	TZ (ppm)	s.e. (TZ)
Li	1.32	0.01	1.31	0.03
Al	0.65	0.14	b.d.	b.d.
P	67.38	1.01	40.94	0.88
Ti	6.81	0.04	2.92	0.06
Y	464.1	0.9	122.6	0.3
Nb	4.20	0.01	0.370	0.004
Ba	b.d.	b.d.	b.d.	b.d.
La	b.d.	b.d.	b.d.	b.d.
Ce	2.240	0.002	2.890	0.002
Pr	0.050	0.001	b.d.	b.d.
Nd	0.750	0.009	1.59	0.02
Sm	1.86	0.01	2.72	0.04
Eu	1.550	0.004	1.67	0.01
Gd	12.17	0.03	9.25	0.07
Tb	4.330	0.006	2.07	0.01
Dy	51.89	0.07	17.42	0.07
Ho	17.18	0.02	4.40	0.02
Er	71.33	0.21	15.16	0.06
Tm	12.71	0.05	2.44	0.01
Yb	97.81	0.51	18.80	0.07
Lu	16.48	0.12	3.29	0.02
Hf	5207	8	5584	19
Ta	1.74	0.01	0.110	0.001
Pb	b.d.	b.d.	1.67	0.01
Th	40.73	0.04	30.51	0.08
U	74.81	0.19	27.30	0.06

2.2.4. X-ray absorption near-edge structure (XANES) spectroscopy

Ti K-edge X-ray absorption near-edge structure (XANES) spectra were recorded in fluorescence mode at beamline 13-ID-E (GSECARS) of the Advanced Photon Source at Argonne National Laboratory (Chicago, USA). The excitation energy was selected using a cryogenically cooled Si(111) monochromator, with the energy calibrated by defining the first derivative peak of the spectrum of Ti metal foil (recorded in transmission mode) to be at 4966 eV. The beam was focused to a 1×2 μm spot, and high-energy harmonics removed using Rh-coated Kirkpatrick-Baez mirrors. Spectra were recorded from 4866 to 5430 eV, with variable step sizes: 4866-4955 eV: 5 eV; 4955-5000 eV: 0.1 eV; 5000-5150 eV: 1 eV and 5150-5430 eV: 10 eV. The sample surface was positioned at 45° to both the incident beam and a Si-drift fluorescence detector (Hitachi Vortex ME4). The counts from the detector were processed using Quantum Xspress3 digital signal electronics and corrected for detector dead time. Spectra were normalized to the incident photon flux measured upstream of the focusing mirrors. Spectra were normalized using Athena (Ravel and Newville 2005) to the average intensity above 5043 eV.

The samples were presented in the same epoxy mounts used for LA-ICP-MS, such that the diffusion interface was parallel to the plane defined by the incident beam and the detector. Spectra were recorded from samples VZ_ZTBSC3 and VZ_ZQRC3. The orientation of the samples relative to the beam, along with the assumption that diffusion can be approximated as one-dimensional, means that each XANES spectrum represents a ∼2 μm wide section of the diffusion profile. A series of spectra were recorded at different distances from the crystal-powder interface for each sample.

2.2.5. Focused ion beam (FIB) sample preparation

For Transmission Electron Microscopy (TEM) a thin, electron-transparent lamella was prepared using the FEI Helios 600i focused ion beam scanning electron microscope (FIB/SEM) housed in the

Scientific Center for Optical and Electron Microscopy (ScopeM) at ETH Zurich. To preserve the area of interest from the ion beam, a protective layer of carbon was deposited. A focused beam of Ga ions, accelerated at 30 kV with a beam current of 21 nA, was used to cut out a lamella (approximate size: 20 µm × 10 µm × 3 µm) of the bulk material bordering the diffusion interface. The lamella was lifted from the bulk material and put onto a Cu TEM half grid. Milling the lamella down to electron transparency on the TEM half grid was done in several steps using Ga ion beams at acceleration voltages of 30 kV, 8 kV and 5 kV, and corresponding smaller beam currents to limit sample amorphization and implantation of Ga into the sample.

2.2.6. Transmission electron microscopy (TEM)

TEM imaging was done using the FEI Talos F200X transmission electron microscope housed in ScopeM at ETH Zurich. The microscope was used with an acceleration voltage of 200 kV. Prior to the TEM measurements, the FIB-prepared lamella was cleaned using a Hitachi Zone TEM Cleaner. Hydrocarbon contamination was removed from the sample surface using an Ar O plasma and UV radiation, and thus allows high resolution imaging without being compromised by resolution-diminishing contamination built up under the influence of the electron beam. Most measurements were done in scanning transmission electron microscopy (STEM) mode. To verify the orientation of the crystal, Selected Area Electron Diffraction (SAED) was used. Indexing of diffraction patterns was done using SingleCrystal of the CrystalMaker Software.

2.3. Diffusion modeling

For concentration-dependent diffusion within a plane-sheet geometry, the relevant diffusion equation is

$$\frac{\partial C(x,t)}{\partial t} = \frac{\partial D(C)}{\partial x} \times \frac{\partial C(x.t)}{\partial x} + \frac{\partial^2 C(x.t)}{\partial x^2} \quad (1)$$

Where D is the diffusion coefficient, t is time, C is concentration and x is distance. In this study we employed an explicit finite-difference scheme to model experimental profiles, such that upon discretization Eq. (1) becomes

$$C_{i,j+1} = C_{i,j} + \Delta t\left(\frac{D_{i+1,j} - D_{i,j}}{\Delta x}\right)\left(\frac{C_{i+1,j} - C_{i,j}}{\Delta x}\right) + D_{i,j}\Delta t\left(\frac{C_{i+1,j} - 2C_{i,j} + C_{i-1,j}}{\Delta x^2}\right) \quad (2)$$

where Δx and Δt represent the distance and time step sizes, respectively. The i and j subscripts in Eq. (2) are integers representing the time and distance points, respectively, on the numerical grid (Costa et al., 2008). The diffusion coefficients were varied as several different functions of concentration, but the best fits were obtained from a simple linear concentration dependence such that

$$\log D = \log D_{max} - \Delta \log D\left(\frac{C(x,t) - C_{inf}}{C_S - C_{inf}}\right) \quad (3)$$

where $\log D_{max}$ is the base-10 logarithm of the highest diffusion coefficient needed for a given model fit, $\Delta \log D$ is the total variation of logD throughout the profile, C(x,t) = concentration at point x and time t, C_S = fixed surface concentration and C_{inf} = homogenous initial background concentration. Although the normalized concentration dependence described by Eq. (3) has the disadvantage that our results cannot be used to obtain a general expression for the dependence of Ti diffusivity on absolute Ti concentration, this approach was necessary due to the fact that profiles determined by SIMS depth profiling and NanoSIMS step scanning were not standardized to produce absolute Ti concentrations. Nonetheless, the observed concentration dependence is small and has an almost negligible impact on the retrieved parameters for Ti diffusion in zircon. Profiles were modeled by linking Eqs. (2) & (3) with a non-linear least-squares optimization routine implemented in MATLAB. Uncertainties were estimated by systematically varying the relevant model parameters to visually estimate minimum and maximum values that could still produce acceptable fits to the data.

3. Results

3.1. Diffusion of Ti in zircon

3.1.1. Concentration dependence

Examples of experimental Ti diffusion profiles produced in this study are shown in Fig. 2. Most profiles could not be fit satisfactorily using a standard (*e.g.* single, concentration-independent diffusion mechanism) analytical diffusion model. The concentration gradients of Ti tend to become too steep towards the diffusion interface to correspond to a simple error function, which indicates that Ti diffusion in zircon may be a function of its own concentration. Instead, the observed profiles were well fit using Eqs. (2) & (3), as illustrated in Fig. 2. In the majority of the samples, the total change in diffusion coefficient across the entire measured profile was less than 0.5 log units. Every profile in which the change in diffusion coefficient exceeds 0.5 log units came from an experiment that was performed above 1300 °C. The maximum change in diffusion coefficient within a single profile was 0.89 log units (at 1500 °C).

3.1.2. Major element activities and oxygen fugacity

Within the uncertainties of the retrieved diffusion parameters, there is no resolvable dependence of Ti diffusion in zircon upon $aSiO_2$ or $aZrO_2$. In both Zrn-Bdy-Sri and Zrn-Crs-Rt buffering/source powders, $aSiO_2$ and $aZrO_2$ are buffered by the reaction

$$SiO_2 + ZrO_2 = ZrSiO_4 \quad (4)$$

Across the range of experimental temperatures imposed in this study (1100 – 1540 °C), the $aSiO_2$ of the Zrn-Bdy-Sri buffering/source powder varies from 0.36 – 0.58. The $aSiO_2$ (and $aZrO_2$) imposed by the Zrn-Sri-Rt powder could not be calculated reliably due to the lack of thermodynamic data for srilankite within internally consistent thermodynamic databases, but it should be intermediate between that of Zrn-Bdy-Sri and Zrn-Crs-Rt ($aSiO_2$ = 1). For the experiments buffered by Zrn-Crs-Rt powders, $aZrO_2$ also varies from 0.36-0.58 and the $aZrO_2$ of the Zrn-Sri-Rt powders is intermediate between Zrn-Crs-Rt and Zrn-Bdy-Sri ($aZrO_2$ = 1). Calculations of $aSiO_2$ and $aZrO_2$ were made using the internally consistent thermodynamic database of Holland and Powell (2011), assuming end-member compositions.

Although $aTiO_2$ also does not appear to exert a strong influence on Ti diffusivity, experiments in which the source powders did not include a Ti phase (*i.e.*, rutile or srilankite) generally produced the least variation in Ti diffusion coefficient across the diffusion profiles. This is an expected result within the framework of a concentration-dependent diffusion model, because these experiments resulted in the smallest change in absolute Ti concentration within the diffusion zone. There is no resolvable dependence of Ti diffusion in zircon upon oxygen fugacity between experiments run in air and at fO_2 corresponding to Ni-NiO, i.e. a difference in fO_2 of ~4.3 log units at 1500 °C.

3.1.3. Time-series experiments

Time-series experiments for Ti diffusion in zircon were carried out at 1200 and 1300 °C (Fig. 3) and were conducted to observe

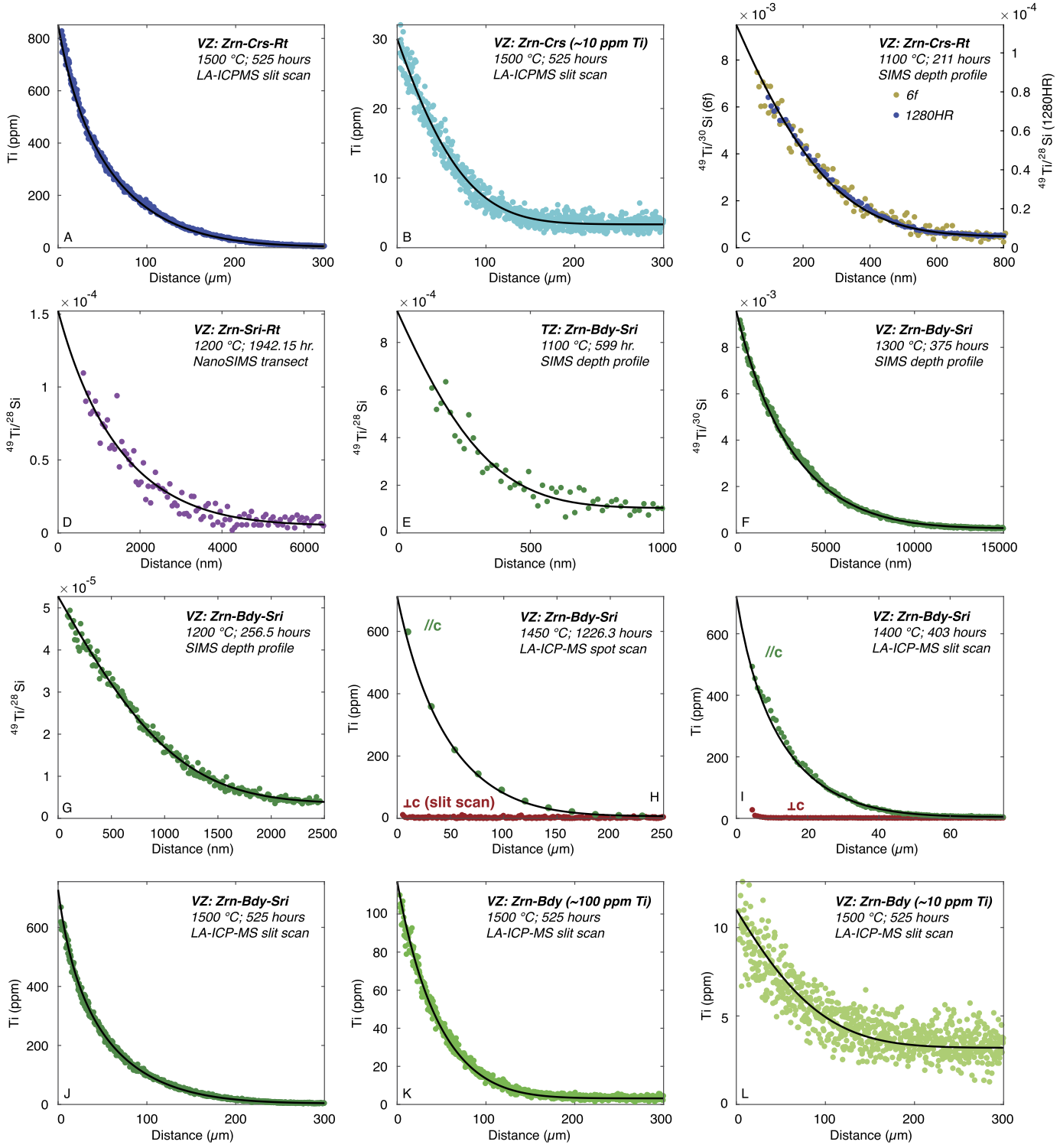

Fig. 2. Representative diffusion profiles produced in this study. All profiles were measured parallel to the c-axis unless otherwise noted. Samples were analyzed by SIMS depth profiling, LA-ICP-MS slit-scanning & spot transects, and NanoSIMS step-scanning. The stable phase assemblage of the Ti source powder and analytical technique used in each experiment is labeled, along with the temperature and duration of the experiments. Model fits are solid lines, obtained using Eqs. (2) and (3) from the main text. See Fig. 1 or Table 1 for mineral abbreviations. The color of the data points in each panel represents the source powder used in that experiment (as in Fig. 1).

diffusion parallel to the c-axis. Time-series experiments at 1200 and 1300 °C spanned factors of 42.2 and 18.5 in run time, respectively. Neither time-series yields any resolvable dependence of Ti diffusivity in zircon upon experimental duration. Values plotted in Fig. 3 correspond to the diffusion coefficient at median Ti concentration, listed as $\log D_{eff}$ in Table 1 ($\log D_{max} - \Delta \log D/2$).

3.1.4. Temperature dependence and diffusion anisotropy

Because there is no resolvable dependence of Ti diffusion in zircon on major element activities or oxygen fugacity, all of the diffusion coefficients determined in this study were used to define a single Arrhenius trend. Diffusion parameters for Ti in zircon were defined using the diffusion coefficient corresponding to the

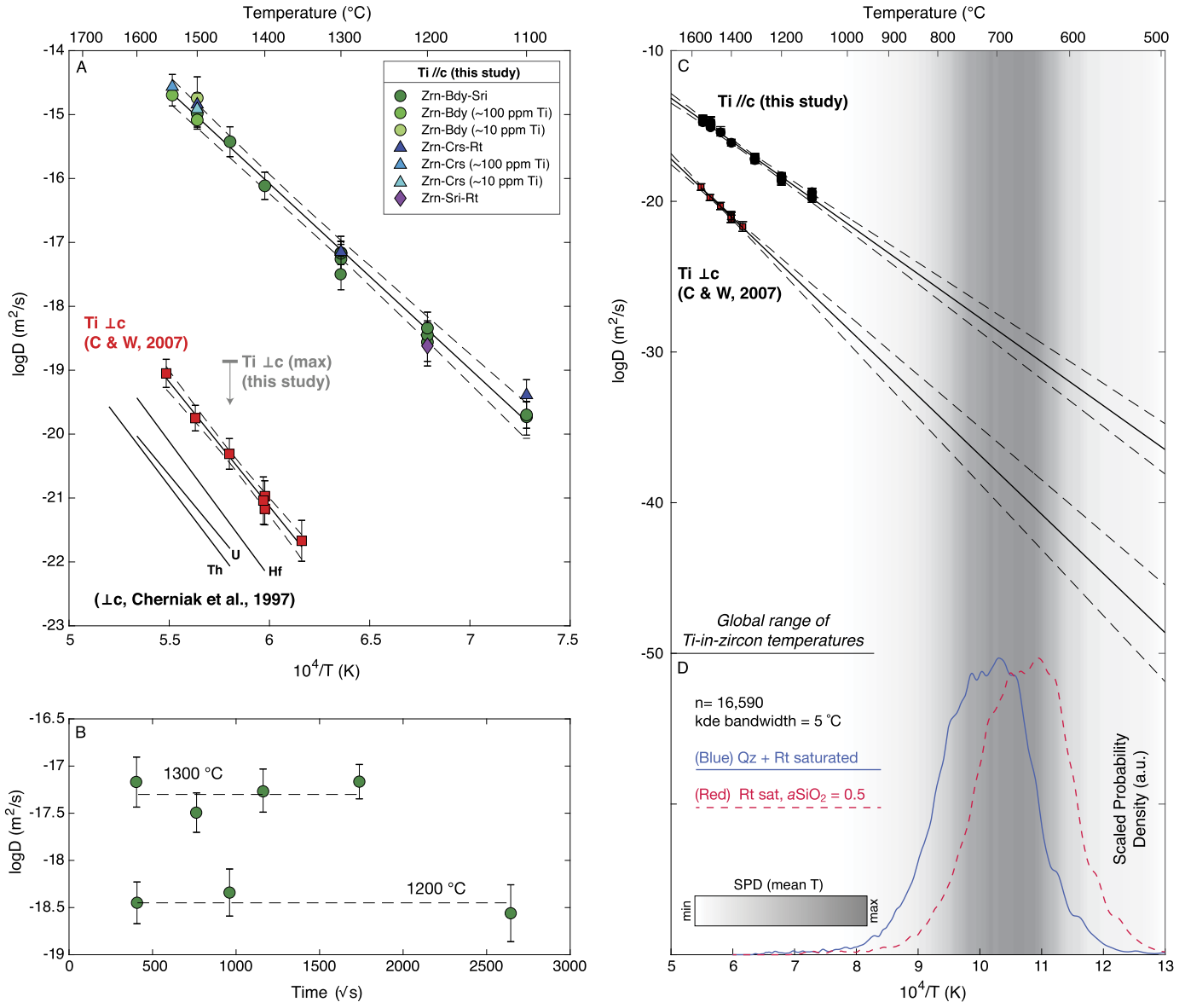

Fig. 3. Arrhenius plots and the results of time-series experiments. A: Diffusion coefficients determined Ti diffusion parallel to the c-axis in zircon and a maximum diffusion coefficient for Ti perpendicular to the c-axis from this study (plotted values are $\log D_{eff}$ from Table 1). The solid line is the best fit to the data (Eq. (5)), and the dashed lines indicate the associated uncertainty envelopes (calculated after (Browaeys, 2021), and approximated by Eqs. (6) and (7)). Also shown are the diffusion coefficients reported by Cherniak and Watson (2007) for Ti diffusion perpendicular to the c-axis in zircon (red data and lines as defined for the data from the present study), and Arrhenius trends reported by Cherniak et al. (1997a) for U, Th and Hf diffusion perpendicular to the c-axis in zircon. See Fig. 1 or Table 1 for mineral abbreviations. B: Diffusion coefficients at median Ti concentration, determined at 1200 and 1300 °C, as a function of time. C: Extrapolation of the data determined in this study and that of Cherniak and Watson (2007) to 500 °C. D: Temperatures calculated from 16,590 Ti-in-zircon concentrations, obtained from the GEOROC (2021) database (http://georoc.mpch-mainz.gwdg.de/georoc, state: 15 January 2021). The blue (solid) and red (dashed) curves show temperatures calculated according to Ferry and Watson (2007) with $aSiO_2 = aTiO_2 = 1$; and $aSiO_2 = 0.5$ & $aTiO_2 = 1$, respectively. The shaded region shows the average temperatures taken from the two sets of calculations.

median Ti concentration in each experimental profile ($\log D_{max} - \Delta\log D/2$). The data were fit, and the error envelopes calculated, using a Monte Carlo scheme (Browaeys, 2021) (Fig. 3A). Taking this approach, diffusion of Ti in zircon parallel to the c-axis at 1 atm pressure is described by

$$\log_{10} D_{Ti} = \left[1.34(\pm 1.44) - \frac{555425(\pm 44820)\ \mathrm{J\,mol^{-1}}}{2.303\ RT\ (K)}\right] \mathrm{m^2\,s^{-1}} \quad (5)$$

where R is the gas constant in J/mol·K. Within the temperature range of 1800-450 °C, the minimum and maximum Ti diffusivities within the uncertainty limits of Eq. (5) are well approximated by the respective polynomial fits

$$\log_{10} D_{Ti,min} = \left[-0.001265\left(\frac{10000}{T\ (K)}\right)^4 + 0.05128\left(\frac{10000}{T\ (K)}\right)^3 - 0.7689\left(\frac{10000}{T\ (K)}\right)^2 + 1.895\left(\frac{10000}{T\ (K)}\right) - 9.365\right] \mathrm{m^2/s} \quad (6)$$

and

$$\log_{10} D_{Ti,max} = \left[0.001057\left(\frac{10000}{T\ (K)}\right)^4 - 0.04361\left(\frac{10000}{T\ (K)}\right)^3 + 0.6663\left(\frac{10000}{T\ (K)}\right)^2 - 7.118\left(\frac{10000}{T\ (K)}\right) + 10.85\right] \mathrm{m^2/s} \quad (7)$$

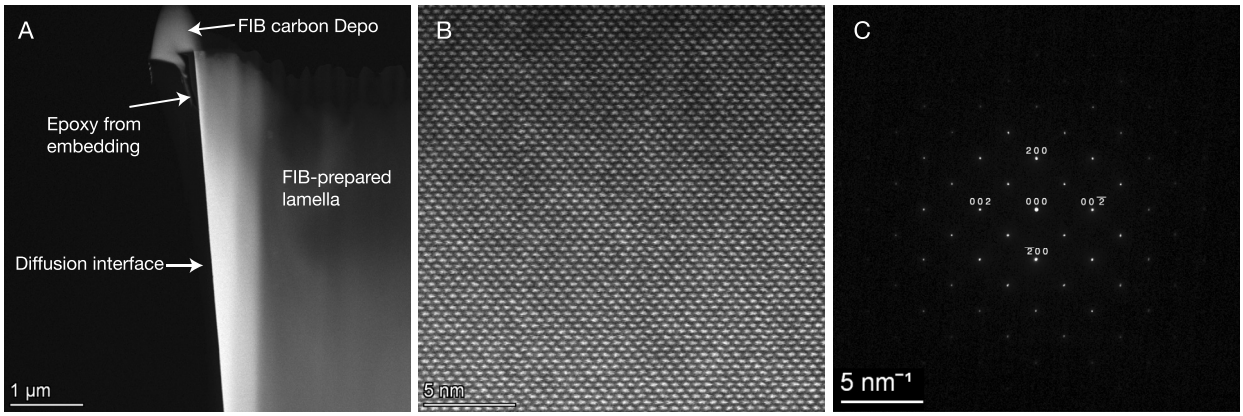

Fig. 4. Representative TEM images from sample VZ_ZTBSC4. A: High angle annular dark field (HAADF) STEM image showing FIB-prepared zircon lamella, which includes the diffusion interface after the experiment was completed and the powder source was removed. B: High-resolution STEM image obtained within 1 µm of the diffusion interface. C: SAE diffraction pattern from the region in B.

Only two experiments were conducted in this study such to investigate diffusion perpendicular to the c-axis. In both of those experiments (Fig. 2, panels H & I), the resulting diffusion profile was too short to be measured by LA-ICP-MS or NanoSIMS and therefore only maximum diffusivities could be obtained; however, the maximum diffusivities from these experiments are consistent with the experimental study of Cherniak and Watson (2007), in which Ti diffusion in zircon was examined perpendicular to the c-axis. In the following discussion, we therefore we use the data reported by Cherniak and Watson (2007) in order to assess the extent of Ti diffusion anisotropy in zircon (Fig. 3).

3.2. Transmission electron microscopy imaging

One of the samples (VZ_ZTBSC4) was imaged by TEM after the experimental diffusion profile was measured by LA-ICP-MS. The Ti diffusion profile from this sample was ~200 µm long (Fig. 2H), and both the high-resolution STEM image (Fig. 4B) and SAE diffraction pattern (Fig. 4C) were recorded within 1 µm of the diffusion interface. These images reveal no evidence of linear or planar defects that could have resulted in accelerated Ti diffusion parallel to the c-axis, nor partial amorphization resulting from residual radiation damage.

3.3. X-ray absorption near-edge structure spectroscopy

XANES spectra were recorded for two samples (VZ_ZTBSC3 and VZ_ZQRC3). These samples were chosen because the measured Ti profiles were among the longest and have the highest concentrations of those produced in this study (Fig. 2, panels A & J), and therefore are ideal to determine the Ti site occupancy during diffusion in zircon. Ti K-edge XANES spectra are shown in Fig. 5A. The energy and intensity of the pre-edge feature at ~4968 eV is diagnostic of the coordination of Ti (Berry et al., 2007; Farge et al., 1996; Tailby et al., 2011). Also shown in Fig. 5A are model spectra for $^{[IV]}$Ti and $^{[VIII]}$Ti in zircon reported by Tailby et al. (2011).

4. Discussion

4.1. Ti incorporation and concentration dependence of diffusion

The XANES spectra (Fig. 5) recorded near the diffusion interface is characteristic of $^{[IV]}$Ti, whereas those from points far removed from the source of Ti suggest the presence of a more highly coordinated component in addition to $^{[IV]}$Ti. The systematic variation in the spectra with distance from the interface can be modeled almost perfectly as a linear combination of the interface and background spectra (Fig. 5, panels B & C). The background spectrum corresponds to the ~3-7 ppm Ti that was present in the crystal initially (Table 2) and its contribution to the XANES spectra only becomes noticeable when the concentration of the diffusing species approaches that of the background (Fig. 5C). The XANES spectra indicate that there is only one diffusing species and that it is $^{[IV]}$Ti.

The structure of zircon is relatively open, with multiple structural voids that are potential interstitial sites capable of incorporating trace elements. One of these interstices is a tetrahedrally coordinated site, located 1.84 Å from four adjacent O sites (Finch and Hanchar, 2003), which occupies open channels parallel to the c-axis (Fig. 6). Due to the similarity between this interstitial site and the Si-site in zircon, it is likely that $^{[IV]}$Ti occupying these sites would produce similar XANES spectra. Extended X-ray absorption fine structure (EXAFS) spectra determine a Ti-O bond distance in zircon of 1.76 Å (Tailby et al., 2011), which indicates that the tetrahedral interstitial site in zircon described above is likely to be highly favorable for Ti. We therefore find it likely that Ti is incorporated into this tetrahedrally coordinated interstitial site in zircon, associated with a Si- and/or Zr-site vacancy to satisfy charge balance, but it is also possible that Ti substitutes directly onto the Si-site and simply utilizes the interstitial sites for diffusion hops.

The measured Ti in zircon diffusion profiles are best fit with a model in which $\log_{10}D_{Ti}$ is negatively and linearly correlated with Ti concentration (Eq. (3)). The observed concentration dependence is generally weak, with the Ti diffusion coefficient varying by less than 0.5 log units across every profile from a sample run below 1300 °C. This concentration dependence therefore has little consequence for application of our data to modeling natural systems. It is possible that the concentration dependence is related to interstitial Ti satisfying charge balance by associating with Si and Zr vacancies in changing proportions correlated with Ti concentration, but this is not entirely clear. Although we have not observed any dependence of Ti diffusion upon oxygen fugacity, we note that we did not conduct experiments at low enough fO_2 for significant Ti^{3+} to be present. Such low fO_2 conditions are rarely encountered on Earth, but could be relevant if our results are applied to extraterrestrial samples (*e.g.*, Borisov, 2012).

4.2. Diffusion anisotropy

The data obtained in this study show significantly faster diffusion of Ti in zircon than observed in previous studies, and reveal a large degree of diffusion anisotropy. Within the temperature range investigated both in this study and by Cherniak and Watson (2007)

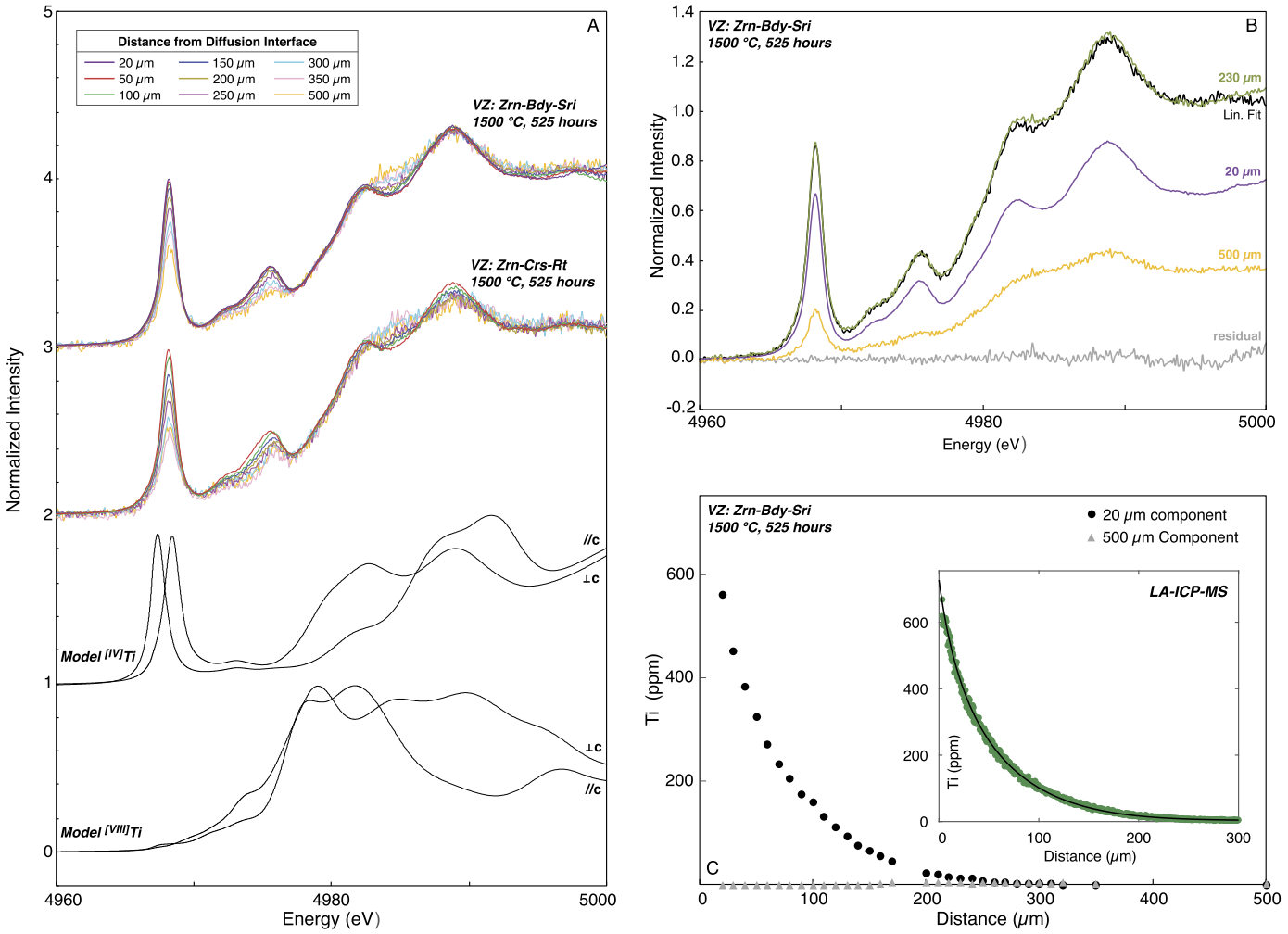

Fig. 5. Representative Ti K-edge XANES spectra from two samples. A: XANES spectra recorded at various distances from the diffusion interfaces. Also shown are the model Ti K-edge XANES spectra for $^{[IV]}$Ti and $^{[VIII]}$Ti in zircon reported by Tailby et al. (2011), normalized to maximum intensity, for X-rays polarized parallel and perpendicular to the c-axis. Spectra are offset for clarity. B: Spectrum from near-rim (20 μm from diffusion interface), background spectrum (500 μm from diffusion interface) and an intermediate position along the profile (230 μm from the diffusion interface). All intermediate spectra can be reproduced by a linear combination of the near-rim and background spectra. C: Relative abundance of each component across the entire profile, illustrating that the background component does not significantly contribute to Ti diffusion in zircon. Relative contributions of each component were calculated as shown in (B), and calibrated against LA-ICP-MS measurements of absolute Ti concentrations (inset).

(1350 – 1540 °C), Ti diffusion in zircon differs by ~4-5 orders of magnitude depending on the orientation of the crystal, with faster diffusion occurring parallel to the c-axis (Fig. 3A). This difference between Ti diffusion coefficients parallel and perpendicular to the c-axis becomes even larger when the data are extrapolated to lower temperatures, relevant to igneous zircon crystallization (Fig. 3C). The possibility that the observed diffusivity parallel to the c-axis was enhanced by zircon breakdown, radiation damage or c-axis aligned linear/planar defects, can be confidently ruled out based on TEM imaging (Fig. 4), Raman spectra (Fig. S1) and consistent results obtained from two separate stocks of zircon. We consider the most likely explanation for the observed diffusion anisotropy to be that Ti in zircon is able to exploit the open channels parallel to the c-axis (Fig. 6), on which the tetrahedral interstitial sites described above are located (Finch and Hanchar, 2003), for fast diffusion.

4.3. Other variables that may influence Ti diffusion (pressure, radiation damage and water fugacity)

Although we have not reported data from any experiments run at elevated pressures, the c-axis aligned interstitial sites (Fig. 6) that presumably act as fast-diffusion paths are not significantly diminished within the P-T space relevant for most naturally occurring zircons. The zircon structure, with its interstitial sites, is stable until it undergoes a polymorphic transition to reidite above ~5 GPa (Hazen and Finger, 1979; Timms et al., 2017). Determining the activation volume of Ti diffusion in zircon parallel to the c-axis would be useful for studies aimed at high-pressure zircons (*e.g.*, Greenough et al., 2021); however, this was not a priority in this study due to the fact that most zircons originate from Si-rich rocks in the Earth's shallow crust, where pressure is unlikely to make a significant impact on diffusivity.

Another variable that could impact the observed diffusion anisotropy of Ti in zircon is radiation damage. Helium diffusion in low-damage zircon exhibits a high degree of anisotropy, with faster diffusion observed parallel to the c-axis, which is also attributed to the interstitial sites that form open channels in this direction (Fig. 6). However, it has been shown that accumulating radiation damage inhibits He diffusion parallel to the c-axis, due in part to increased blockage/tortuosity of these channels (*e.g.*, Anderson et al., 2020; Cherniak, 2019; Guenthner et al., 2013). Although it seems plausible that significant radiation damage could also decrease Ti diffusivity parallel to the c-axis, the temperatures of interest for Ti diffusion in zircon are significantly higher (over at least ~600 °C, probably higher as discussed below) than those of

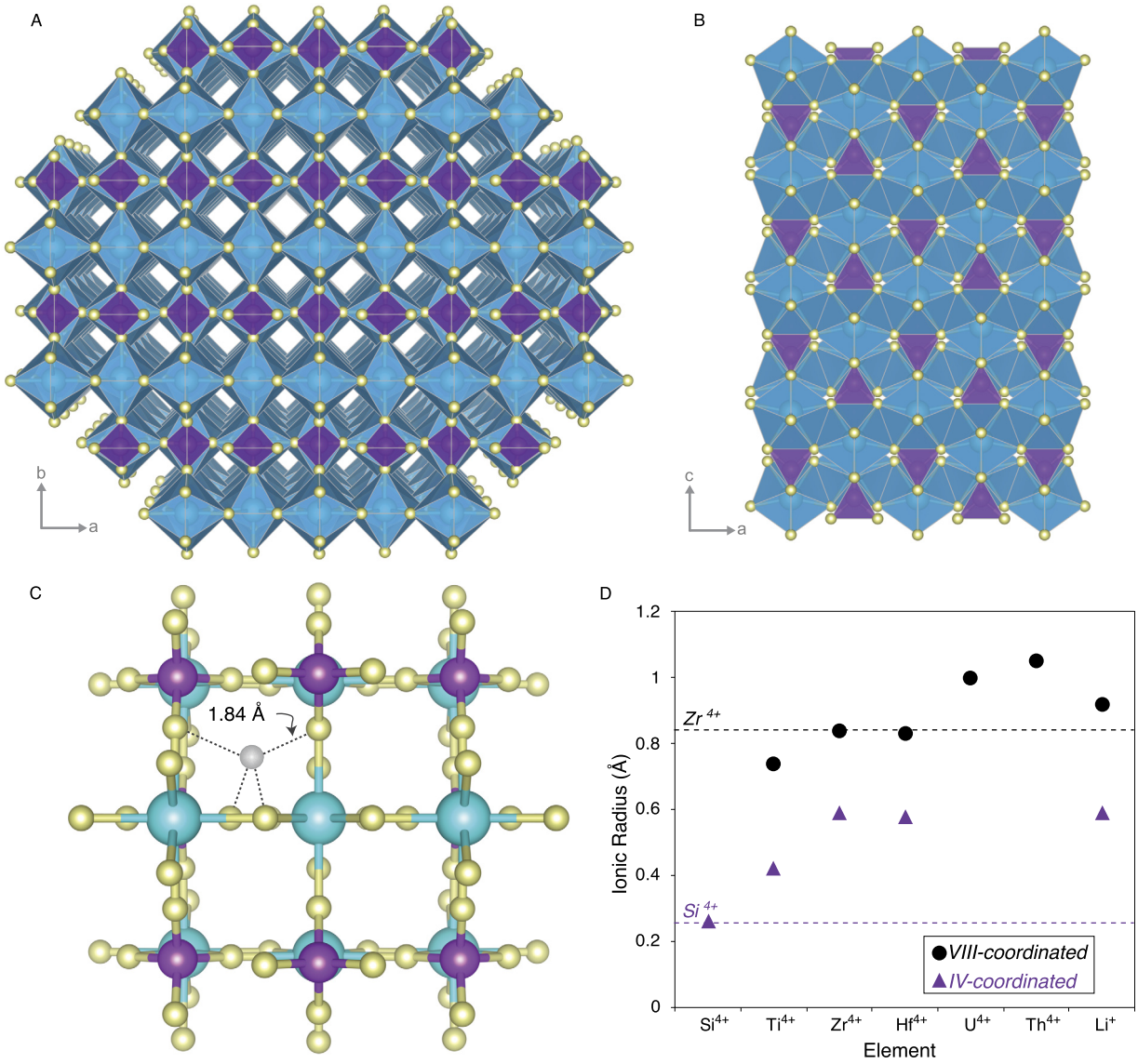

Fig. 6. A: Projection of the zircon structure onto the a-b plane, illustrating the open channels parallel to the crystallographic c-axis. B: Projection of the zircon structure onto the a-c plane. Blue dodecahedra represent $^{[VIII]}Zr^{4+}$, purple tetrahedra represent $^{[IV]}Si^{4+}$ and yellow spheres represent O^{2-}. Images were drawn using the software package VESTA (Momma and Izumi, 2011). C: Zircon structure viewed down the c-axis (same orientation as panel A), showing the IV-coordinated interstitial site that lies within the open channels parallel to the c-axis (after Finch and Hanchar (2003)). Blue, purple, yellow and gray spheres represent Zr, Si, O and interstitial sites, respectively. D: Ionic radii of several cations of interest, in tetrahedral and dodecahedral coordination, from Shannon (1976). Horizontal dashed lines intersect Si and Zr.

interest for He thermochronology (typically less than ~200 °C) or those required for significant accumulation of radiation damage in a cooling igneous zircon. Therefore, even though the kinetics of radiation damage annealing are complicated, particularly for zircon that have resided at low temperature for long enough to accumulate significant α recoil damage (Ginster et al., 2019), it seems unlikely that radiation damage is a major concern for Ti diffusion in zircon. Furthermore, without independent data it is hard to draw a direct comparison between the systematics of a noble gas such as He and those of a high field strength element such as Ti.

It has been shown that increased water fugacity (fH_2O) is associated with enhanced cation diffusivity in some systems (Graham and Elphick, 1991; Hier-Majumder et al., 2005; Yund and Snow, 1989), whereas it appears negligible in others (Jollands et al., 2016). Although Cherniak and Watson (2007) did not observe a difference in Ti diffusivity perpendicular to the c-axis between anhydrous experiments and experiments run with a fluid phase present, it is still possible that Ti diffusion parallel to the c-axis may be influenced by fH_2O. Because all experiments reported here were run under anhydrous conditions, experiments varying fH_2O should clarify this issue in future studies.

4.4. Extrapolation of Ti-in-zircon diffusion data to geologically relevant temperatures

Although the experiments presented in this study were conducted over a larger temperature range (1540-1100 °C) than those of Cherniak and Watson (2007) (1550-1350 °C), application of either dataset to natural zircons in most cases still requires extrapolation to significantly lower temperatures. To illustrate this problem, temperatures were calculated from 16,590 Ti-in-zircon measurements, compiled from the GEOROC (2021) database (http://georoc.mpch-mainz.gwdg.de/georoc, state: 15 January 2021). All Ti analyses present in the pre-compiled 'ZIRCONS.csv' zircon mineral file were used to calculate temperatures. Two sets of calculations were made according to Ferry and Watson (2007) in order to encompass a reasonable range in temperature covered by natural zircon data, (1) imposing $aSiO_2 = aTiO_2 = 1$, and (2) imposing $aSiO_2$

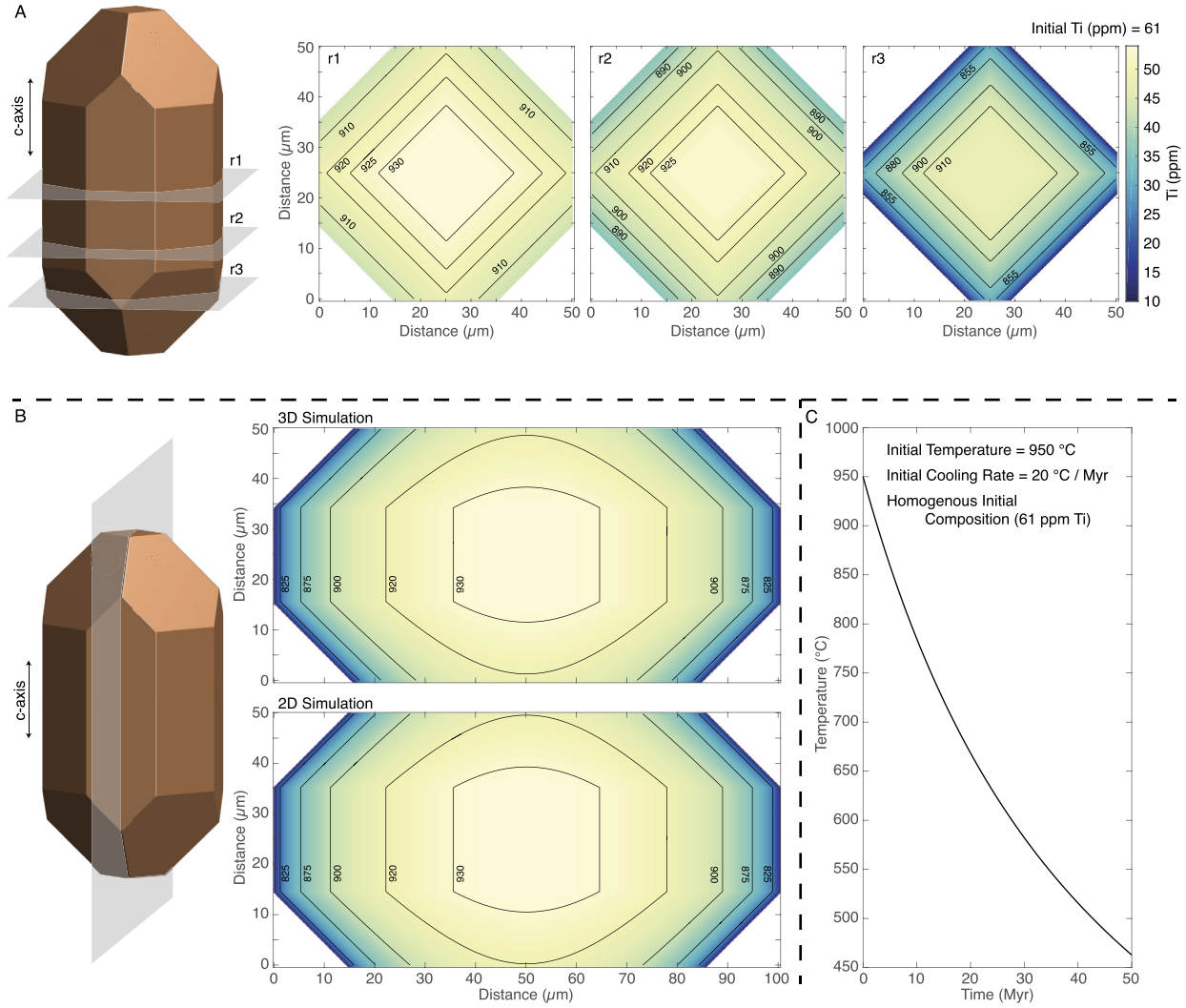

Fig. 7. Three-dimensional simulation of the development of Ti diffusion profiles in zircon. A: C-axis perpendicular (radial) slices taken from the indicated positions (r1, r2 and r3). B: C-axis parallel (longitudinal) cross-section taken through the center of the zircon, as indicated. Also shown in B is a two-dimensional simulation in which the same slice was taken prior to diffusion modeling, but imposing otherwise identical conditions. The color gradient representing Ti is the same scale for each panel, and the contours indicate the temperature that would be calculated from Ti-in-zircon thermometry according to Ferry and Watson (2007). This simulation imposed a peak temperature of 950 °C and cooling through an asymptotic cooling path with an initial cooling rate of 20 °C/ Myr (panel C).

= 0.5 and $aTiO_2$ = 1. The temperatures resulting from each set of calculations, and the average between them, are shown in Fig. 3, panels C & D. Although reported Ti-in-zircon temperatures close to the range of temperatures used to experimentally constrain Ti-in-zircon diffusivities are not exceedingly rare (*e.g.*, Baldwin et al., 2007; Stepanov et al., 2016), the vast majority fall in the range of ~600 - 800 °C, which requires a minimum of 300 °C extrapolation.

There are two potentially significant issues that arise with large extrapolations of diffusion data to lower temperatures, the first of which is uncertainty propagation. Uncertainty envelopes become larger as the extrapolation increases. For diffusion of Ti in zircon parallel to the c-axis, there are ~1.6 and 2.7 orders of magnitude uncertainty in D_{Ti} at 800 and 600 °C, respectively (Fig. 3C). For practical purposes, between 1800 and 450 °C the minimum and maximum permissible values of Ti diffusion parallel to the c-axis in zircon, according to the uncertainties in Eq. (5), are well approximated by the polynomial fits described by Eqs. (6) & (7), respectively, and these uncertainties should be considered whenever applying our experimental results to natural systems. Outside of this temperature range (1800-450 °C) these polynomial fits should not be used, and the uncertainties should be calculated directly from Eq. (5).

The second issue with large extrapolations of diffusion data is that it must be assumed that the Arrhenius trend maintains linearity over the entire temperature range. Although the data presented here and by Cherniak and Watson (2007) shows no resolvable deviation from linearity within the experimental temperature range, there is no guarantee that the Arrhenius trends do not have a kink or curvature at lower temperatures. For example, such a change in activation energy could occur due to a shift from an intrinsic to a pure extrinsic diffusion regime (e.g., Chakraborty, 1997; Dohmen et al., 2007; Dohmen and Chakraborty, 2007). This would tend to lead to faster diffusion than extrapolation of the data reported here indicates, even taking the associated uncertainty into account. Until diffusion data are obtained directly from lower temperature experiments, interpretations of low Ti-in-zircon temperatures should therefore be made with caution.

4.5. Application of Ti diffusion in zircon to Ti-in-Zircon thermometry

Due to the extremely slow diffusion of Ti in zircon previously reported by Cherniak and Watson (2007), it has been reasonably argued that Ti concentrations in zircon cannot be significantly modified by volume diffusion under essentially any crustal con-

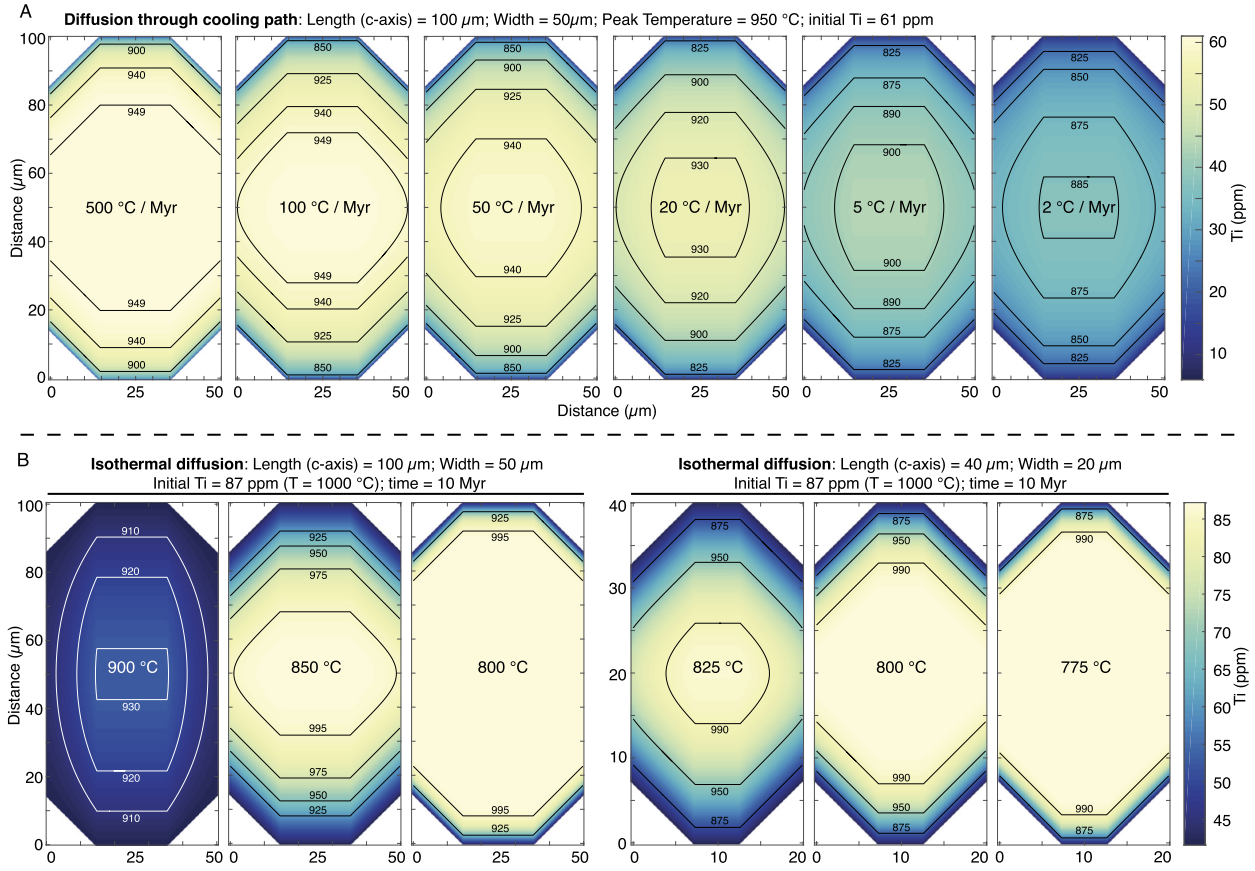

Fig. 8. Two-dimensional simulations of the development of Ti diffusion profiles in zircon. A: Diffusion through an asymptotic cooling path ($1/T = 1/T_P + \eta t$, where T_P = peak temperature and $\eta$is a constant with the dimensions $K^{-1}t^{-1}$). All simulations imposed an initial temperature of 950 °C and $aSiO_2 = aTiO_2 = 1$. Initial cooling rates were varied from 2-500 °C/Myr as indicated on each panel. B: Isothermal diffusion simulations. All calculations impose an initial Ti concentration of 87 ppm (corresponding to 1000 °C at $aSiO_2 = aTiO_2 = 1$). The temperature of isothermal diffusion is indicated on each panel. The color gradient representing Ti is the same scale for each panel (shown on the right of (A) and (B) for each panel therein), and the contours indicate the temperature that would be calculated from Ti-in-zircon thermometry according to Ferry and Watson (2007).

dition encountered on Earth (e.g., Ewing et al., 2013; Fu et al., 2008; Harrison et al., 2007; Hiess et al., 2008). However, from 950-600 °C, the data collected in this study indicate diffusion ~7.5-11 orders of magnitude faster parallel to the c-axis than predicted by the data of Cherniak and Watson (2007) for diffusion perpendicular to the c-axis (Fig. 3C). This large difference in diffusivities clearly indicates that the potential for volume diffusion to modify Ti concentrations in zircon under crustal conditions needs to be re-evaluated.

We have constructed two numerical models to apply the diffusion data obtained in this study and the data of Cherniak and Watson (2007) to anisotropic diffusion in natural zircons. The first model uses a 3-dimensional explicit finite difference scheme to model Ti diffusion in a shape approximating that of euhedral zircon (Fig. 7). The simulation results shown in Fig. 7 assume that zircon grew isothermally at a peak temperature of 950 °C (or was completely re-equilibrated at this peak temperature) before cooling along an asymptotic path with an initial cooling rate of 20 °C/Myr. Throughout the simulation, $aSiO_2 = aTiO_2 = 1$. C-axis perpendicular (radial) and parallel (longitudinal) cross-sections of the final Ti composition are shown in Fig. 7A & B, respectively. The Ti concentration is represented by a color gradient, and the contours represent the temperature (°C) that would be calculated from the Ti-in-zircon thermometer. Boundary conditions throughout cooling and the final temperature contours were calculated according to the calibration of Ferry and Watson (2007). Although imposing different $aSiO_2$ and/or $aTiO_2$ would change the Ti concentrations, as long as they remain constant then the temperature contours would remain the same given D_{Ti} is not dependent upon major element activities. It is interesting to note that although diffusion in the radial direction (Cherniak and Watson, 2007) is essentially negligible, the pyramids at either end of the zircon cause diffusion parallel to the c-axis to create a concentration gradient perpendicular to the c-axis. In this simulation, the peak-temperature Ti composition is not retained at any point within the crystal.

Although the 3D model illustrated in Fig. 7 captures interesting and potentially important consequences of Ti diffusion in zircon using realistic crystal morphologies, this code becomes computationally expensive when high spatial resolution is imposed. We therefore also constructed a similar 2D diffusion model. The 2D model also simulates a realistic zircon morphology, but only in a 2D space parallel to the c-axis and along the center of the crystal. All other aspects of the 2D model are identical to the 3D model, and a comparison between the two is provided in Fig. 7B. Fig. 8 shows several outputs of the 2D model when cooling rate is varied, as well as isothermal diffusion calculations for zircons of different sizes.

Ti-in-zircon has become a very commonly used thermometer, and so it would be unrealistic to perform the number of simulations required to address the wide variety of zircon morphologies and geological settings that this thermometer has been applied to. Instead of including an exorbitant number of such simulations in this manuscript, we have included both the 2D and 3D MATLAB codes in a supplementary file, so that our results can be easily applied to any zircon of interest. The simulations provided in Figs. 7 and 8 illustrate that the Ti concentration of zircon can be modi-

fied by volume diffusion in at least some crustal conditions, and thus diffusive modification of Ti concentrations in zircon should considered on a case-by-case basis, considering both potential T-t paths and zircon size/morphology. Nonetheless, our data indicate that diffusion is not likely to be a major factor in modifying Ti concentrations in most zircons below ~800 °C. At lower temperatures, diffusion appears to only be a significant issue for small zircons (<40 μm, defined either by actual size or an effective diffusion radius imposed by fractures), samples that were very slowly cooled, or samples that experienced long (several tens of millions of years) residence times at high temperatures. The Ti concentrations in the majority of zircons originating from intermediate to felsic igneous systems, or low- to intermediate- grade metamorphic rocks, are therefore unlikely to have undergone major modification by volume diffusion, provided applications of our data do not suffer from additional complexities (sections 4.3 and 4.4).

Although we hope that the diffusion models provided here will prove to be useful tools, users should be aware of two limitations in particular. First, both the 2D and 3D numerical models assume that Ti is free to undergo uninhibited exchange with the matrix surrounding zircon, without other kinetic impediments, with boundary conditions only defined by temperature, $a\mathrm{SiO_2}$ and $a\mathrm{TiO_2}$. In a natural system, if instead zircon is in contact with, or enclosed within, phases in which Ti is slow diffusing, then Ti exchange will of course be limited. Under such conditions, the provided models will overestimate the extent of diffusive modification (and underestimate the calculated Ti temperatures in the case of out-diffusion of Ti, or vice-versa). The second limitation is that these models assume an initially homogenous Ti composition. The physical implication of this assumption is that the zircon either grew, or was subsequently homogenized, under isothermal conditions at fixed $a\mathrm{SiO_2}$ and $a\mathrm{TiO_2}$. These codes could be modified to include crystal growth and resulting Ti growth-zoning profiles, but due to the difficulty in developing a general growth model that is widely applicable to most natural systems, we have not attempted to include growth in these models. Whether the data reported in this study are implemented through the models we have provided or are used elsewhere, calculations aimed at (1) systems requiring a significant extrapolation of the data to lower temperatures, (2) zircons that are suspected to have accumulated significant radiation damage prior to or at the time of Ti diffusion, (3) systems that include a fluid phase, and/or (4) high-P systems, should be interpreted cautiously, as discussed in sections 4.3 and 4.4.

4.6. Implications for diffusion of other tetravalent cations in zircon

Experiments on other tetravalent cations (U, Th, Hf) in zircon have yielded diffusivities even slower than that of Ti in zircon perpendicular to the c-axis (Cherniak et al., 1997a; Suzuki et al., 1992), as shown in Fig. 3A; however, these studies also did not report any results measuring diffusion parallel to the c-axis. The extent of Ti diffusion anisotropy observed in this study, coupled with recent observations from natural zircons that suggest U could diffuse significantly faster than previously recognized (Garber et al., 2020), raises the question of whether other tetravalent cations may show similar diffusion anisotropy in zircon. Faster diffusion of tetravalent cations could have major implications for the interpretation of both U-Pb zircon geochronology, and of Hf and Zr isotopic compositions of zircon.

While the observed diffusion anisotropy of Ti raises important questions for other tetravalent cations, it is not clear at this time whether they will exhibit comparable diffusion systematics. The ionic radii of U, Th, Hf and Zr are considerably larger than that of Ti (Fig. 6C), and it is therefore not clear if they would be able to exploit the interstitial sites within the c-axis-aligned channels (Fig. 6) to the same extent indicated by our data for Ti; however, it is worth noting that Crocombette (1999) calculated point defect energies in zircon and found that some Zr and Si would tend to occupy these sites. Furthermore, it is possible that some or all of the larger tetravalent cations may only be able to exploit these interstitial channels for diffusion at low concentrations. Multiple simultaneously occurring diffusion mechanisms have been reported or suggested for monovalent cations in a number of silicate minerals (Dohmen et al., 2010; Jollands et al., 2020, 2019; Richter et al., 2017, 2014; Sliwinski et al., 2018; Tang et al., 2017), and more recently for Mg^{2+} in sanidine (Shamloo et al., 2021), trivalent cations in garnet (Bloch et al., 2020) and a number of other trace species (Dohmen et al., 2016). This could be particularly consequential for Zr and Hf in zircon, as isotopic ratios could be more susceptible to modification via fast diffusion mechanisms than elemental concentrations, akin to Nd in garnet (Bloch et al., 2020).

5. Conclusions

Diffusion of Ti in zircon shows significant anisotropy, with diffusion parallel to the c-axis occurring orders of magnitude faster than diffusion perpendicular to the c-axis. This diffusion anisotropy is most likely related to interstitial sites that are located on open channels parallel to the c-axis. Diffusion of Ti parallel to the c-axis is weakly dependent on its own concentration within individual profiles, but does not change significantly when $a\mathrm{TiO_2}$ is varied between otherwise identical experiments. There is no resolvable dependence of Ti diffusion on $f\mathrm{O_2}$, $a\mathrm{SiO_2}$ or $a\mathrm{ZrO_2}$.

So long as extrapolation of the reported dataset to significantly lower temperatures is not compromised by additional complexities (e.g., a kink in the Arrhenius trend), then the Ti concentrations in the majority of zircons originating from intermediate to felsic igneous systems, or low- to intermediate-grade metamorphic rocks, are unlikely to have undergone major modification by volume diffusion. Nonetheless, diffusion parallel to the c-axis is fast enough that the reliability of the Ti-in-zircon thermometer for determining zircon crystallization temperatures should be assessed on a case-by-case basis, particularly when evaluating high-T, slowly cooled, reheated and/or small zircons. Furthermore, additional data are needed to clarify the effects of $f\mathrm{H_2O}$, radiation damage and pressure on Ti diffusion in zircon.

CRediT authorship contribution statement

E.M. Bloch: Conceptualization, Data curation, Formal analysis, Funding acquisition, Investigation, Methodology, Resources, Software, Validation, Visualization, Writing – original draft, Writing – review & editing. **M.C. Jollands:** Conceptualization, Formal analysis, Methodology, Software, Writing – review & editing. **P. Tollan:** Investigation, Writing – review & editing. **F. Plane:** Investigation, Writing – review & editing. **A.-S. Bouvier:** Investigation, Writing – review & editing. **R. Hervig:** Investigation, Writing – review & editing. **A.J. Berry:** Formal analysis, Investigation, Writing – review & editing. **C. Zaubitzer:** Formal analysis, Investigation, Writing – review & editing. **S. Escrig:** Investigation, Writing – review & editing. **O. Müntener:** Conceptualization, Writing – review & editing. **M. Ibañez-Mejia:** Formal analysis, Writing – review & editing. **J. Alleon:** Investigation, Writing – review & editing. **A. Meibom:** Investigation, Writing – review & editing. **L.P. Baumgartner:** Conceptualization, Writing – review & editing. **J. Marin-Carbonne:** Conceptualization, Writing – review & editing. **M. Newville:** Investigation, Writing – review & editing.

Declaration of competing interest

The authors declare that they have no known competing financial interests or personal relationships that could have appeared to influence the work reported in this paper.

Acknowledgements

We thank James Watkins, Tanya Ewing, Sumit Chakraborty, Daniela Rubatto, Jörg Hermann and Peter Reiners for constructive discussions throughout the course of this study, as well as Thierry Adatte, Bi Wen Hua and Arnaud Magrez for assistance with powder and single-crystal XRD measurements. We are grateful for a review by Aitor Cambeses and editorial handling by Rajdeep Dasgupta. This research was funded by Ambizione grant PZ00P2_173988 to EB from the Swiss National Science Foundation. The ASU SIMS lab is supported by the US National Science Foundation (EAR – 1819550). Part of this work was performed at GeoSoilEnviro-CARS (The University of Chicago, Sector 13), Advanced Photon Source (APS), Argonne National Laboratory. GeoSoilEnviroCARS is supported by the National Science Foundation – Earth Sciences (EAR – 1634415) and Department of Energy- GeoSciences (DE-FG02-94ER14466). This research used resources of the Advanced Photon Source, a U.S. Department of Energy (DOE) Office of Science User Facility operated for the DOE Office of Science by Argonne National Laboratory under Contract No. DE-AC02-06CH11357.

Appendix A. Supplementary material

Supplementary material related to this article can be found online at https://doi.org/10.1016/j.epsl.2021.117317.

References

Anderson, A.J., van Soest, M.C., Hodges, K.V., Hanchar, J.M., 2020. Helium diffusion in zircon: effects of anisotropy and radiation damage revealed by laser depth profiling. Geochim. Cosmochim. Acta 274, 45–62.

Baldwin, J.A., Brown, M., Schmitz, M.D., 2007. First application of titanium-in-zircon thermometry to ultrahigh-temperature metamorphism. Geology 35.

Berry, A.J., Walker, A.M., Hermann, J., O'Neill, H.S.C., Foran, G.J., Gale, J.D., 2007. Titanium substitution mechanisms in forsterite. Chem. Geol. 242, 176–186.

Bloch, E.M., Jollands, M.C., Devoir, A., Bouvier, A.S., Ibañez-Mejia, M., Baumgartner, L.P., 2020. Multispecies diffusion of Yttrium, rare Earth elements and Hafnium in Garnet. J. Petrol. 61.

Borisov, A.A., 2012. The Ti^{4+}/Ti^{3+} ratio of magmatic melts: application to the problem of the reduction of lunar basalts. Petrology 20, 391–398.

Browaeys, J., 2021. Linear fit with both uncertainties in x and in y. https://www.mathworks.com/matlabcentral/fileexchange/45711-linear-fit-with-both-uncertainties-in-x-and-in-y). MATLAB Central File Exchange.

Chakraborty, S., 1997. Rates and mechanisms of Fe-Mg interdiffusion in olivine at 980 °-1300 °C. J. Geophys. Res., Solid Earth 102, 12317–12331.

Chen, X., Wang, W., Zhang, Z., Nie, N.X., Dauphas, N., 2020. Evidence from ab initio and transport modeling for diffusion-driven zirconium isotopic fractionation in igneous rocks. ACS Earth and Space Chem. 4, 1572–1595.

Cherniak, D.J., 2019. Diffusion of helium in radiation-damaged zircon. Chem. Geol. 529.

Cherniak, D.J., Hanchar, J.M., Watson, B.E., 1997a. Diffusion of tetravalent cations in zircon. Contrib. Mineral. Petrol. 127, 383–390.

Cherniak, D.J., Hanchar, J.M., Watson, E.B., 1997b. Rare-Earth diffusion in zircon. Chem. Geol. 134, 289–301.

Cherniak, D.J., Watson, E.B., 2000. Pb diffusion in zircon. Chem. Geol. 172, 5–24.

Cherniak, D.J., Watson, E.B., 2007. Ti diffusion in zircon. Chem. Geol. 242, 470–483.

Costa, F., Dohmen, R., Chakraborty, S., 2008. Time scales of magmatic processes from modeling the zoning patterns of crystals. Rev. Mineral. Geochem. 69, 545–594.

Crocombette, J.-P., 1999. Theoretical study of point defects in crystalline zircon. Phys. Chem. Miner. 27, 138–143.

Dohmen, R., Becker, H.-W., Chakraborty, S., 2007. Fe–Mg diffusion in olivine I: experimental determination between 700 and 1,200 °C as a function of composition, crystal orientation and oxygen fugacity. Phys. Chem. Miner. 34, 389–407.

Dohmen, R., Chakraborty, S., 2007. Fe–Mg diffusion in olivine II: point defect chemistry, change of diffusion mechanisms and a model for calculation of diffusion coefficients in natural olivine. Phys. Chem. Miner. 34, 409–430.

Dohmen, R., Kasemann, S.A., Coogan, L., Chakraborty, S., 2010. Diffusion of Li in olivine. Part I: experimental observations and a multi species diffusion model. Geochim. Cosmochim. Acta 74, 274–292.

Dohmen, R., Marschall, H.R., Wiedenbeck, M., Polednia, J., Chakraborty, S., 2016. Trace Element Diffusion in Minerals: The Role of Multiple Diffusion Mechanisms Operating Simultaneously. America Geophysical, Union.

Ewing, T.A., Hermann, J., Rubatto, D., 2013. The robustness of the Zr-in-rutile and Ti-in-zircon thermometers during high-temperature metamorphism (Ivrea-Verbano Zone, northern Italy). Contrib. Mineral. Petrol. 165, 757–779.

Farge, F., Brown, G.E., Rehr, J.J., 1996. Coordination chemistry of Ti(IV) in silicate glasses and melts: I. XAFS study of titanium coordination in oxide model compounds. Geochim. Cosmochim. Acta 60, 3023–3038.

Ferry, J.M., Watson, E.B., 2007. New thermodynamic models and revised calibrations for the Ti-in-zircon and Zr-in-rutile thermometers. Contrib. Mineral. Petrol. 154, 429–437.

Finch, R.J., Hanchar, J.M., 2003. Structure and chemistry of zircon and zircon-group minerals. Rev. Mineral. Geochem. 53, 1–25.

Fu, B., Page, F.Z., Cavosie, A.J., Fournelle, J., Kita, N.T., Lackey, J.S., Wilde, S.A., Valley, J.W., 2008. Ti-in-zircon thermometry: applications and limitations. Contrib. Mineral. Petrol. 156, 197–215.

Garber, J.M., Smye, A.J., Feineman, M.D., Kylander-Clark, A.R.C., Matthews, S., 2020. Decoupling of zircon U–Pb and trace-element systematics driven by U diffusion in eclogite-facies zircon (Monviso meta-ophiolite, W. Alps). Contrib. Mineral. Petrol. 175.

Ginster, U., Reiners, P.W., Nasdala, L., Chanmuang, N.C., 2019. Annealing kinetics of radiation damage in zircon. Geochim. Cosmochim. Acta 249, 225–246.

Graham, C., Elphick, S.C., 1991. Some experimental constraints on the role of oxygen and hydrogen diffusion and Al-Si interdiffusion in silicates. In: Ganguly, J. (Ed.), Diffusion, Atomic Ordering and Mass Transport. Springer-Verlag, Berlin, pp. 248–285.

Greenough, J.D., Kamo, S.L., Davis, D.W., Larson, K., Zhang, Z., Layton-Matthews, D., De Vera, J., Bergquist, B.A., 2021. Old subcontinental mantle zircon below Oahu. Commun. Earth Environ. 2.

Grimes, C.B., Wooden, J.L., Cheadle, M.J., John, B.E., 2015. "Fingerprinting" tectonomagmatic provenance using trace elements in igneous zircon. Contrib. Mineral. Petrol. 170.

Guenthner, W.R., Reiners, P.W., Ketcham, R.A., Nasdala, L., Giester, G., 2013. Helium diffusion in natural zircon: radiation damage, anisotropy, and the interpretation of zircon (U-Th)/He thermochronology. Am. J. Sci. 313, 145–198.

Guo, J.L., Wang, Z., Zhang, W., Moynier, F., Cui, D., Hu, Z., Ducea, M.N., 2020. Significant Zr isotope variations in single zircon grains recording magma evolution history. Proc. Natl. Acad. Sci. USA 117, 21125–21131.

Harrison, T.M., Watson, E.B., Aikman, A.B., 2007. Temperature spectra of zircon crystallization in plutonic rocks. Geology 35.

Hazen, R.M., Finger, L.W., 1979. Crystal structure and compressibility of zircon at high pressure. Am. Mineral. 64, 196–201.

Hier-Majumder, S., Anderson, I.M., Kohlstedt, D.L., 2005. Influence of protons on Fe-Mg interdiffusion in olivine. J. Geophys. Res., Solid Earth 110.

Hiess, J., Nutman, A.P., Bennett, V.C., Holden, P., 2008. Ti-in-zircon thermometry applied to contrasting Archean metamorphic and igneous systems. Chem. Geol. 247, 323–338.

Holland, T.J.B., Powell, R., 2011. An improved and extended internally consistent thermodynamic dataset for phases of petrological interest, involving a new equation of state for solids. J. Metamorph. Geol. 29, 333–383.

Hoskin, P.W.O., Schaltegger, U., 2003. The composition of zircon and igneous and metamorphic petrogenesis. Rev. Mineral. Geochem. 53, 27–62.

Huong, L.T.-T., Vuong, B.S., Khoi, N.N., Satitkune, S., Wanthanachaisaeng, B., Hofmeister, W., Häger, T., Hauzenberger, C., 2016. Geology, gemmological properties and preliminary heat treatment of gem-quality zircon from the central highlands of Vietnam. J. Gemmol. 35, 308–318.

Ibañez-Mejia, M., Tissot, F., 2019. Extreme Zr stable isotope fractionation during magmatic fractional crystallization. Sci. Adv. 5, 1–14.

Jollands, M.C., Burnham, A.D., O'Neill, H.S.C., Hermann, J., Qian, Q., 2016. Beryllium diffusion in olivine: a new tool to investigate timescales of magmatic processes. Earth Planet. Sci. Lett. 450, 71–82.

Jollands, M.C., Ellis, B., Tollan, P.M.E., Müntener, O., 2020. An eruption chronometer based on experimentally determined H-Li and H-Na diffusion in quartz applied to the Bishop Tuff. Earth Planet. Sci. Lett. 551.

Jollands, M.C., Kempf, E., Hermann, J., Müntener, O., 2019. Coupled inter-site reaction and diffusion: rapid dehydrogenation of silicon vacancies in natural olivine. Geochim. Cosmochim. Acta 262, 220–242.

Karpe, M., Mezinskis, G., Timma, L., 2014. Synthesis of nanoporous SiO2-TiO2-ZrO2 ceramics using sol-gel technology. Mater. Sci. Appl. Chem. 30.

Méheut, M., Ibañez-Mejia, M., Tissot, F.L.H., 2021. Drivers of zirconium isotope fractionation in Zr-bearing phases and melts: the roles of vibrational, nuclear field shift and diffusive effects. Geochim. Cosmochim. Acta 292, 217–234.

Momma, K., Izumi, F., 2011. VESTA 3for three-dimensional visualization of crystal, volumetric and morphology data. J. Appl. Crystallogr. 44, 1272–1276.

Nye, J., 1985. Physical Properties of Crystals: Their Representation by Tensors and Matrices. Clarendon, Oxford.

Paton, C., Hellstrom, J., Paul, B., Woodhead, J., Hergt, J., 2011. Iolite: freeware for the visualisation and processing of mass spectrometric data. J. Anal. At. Spectrom. 26.

Richter, F., Chaussidon, M., Watson, B., Mendybaev, R., Homolova, V., 2017. Lithium isotope fractionation by diffusion in minerals Part 2: olivine. Geochim. Cosmochim. Acta 219, 124–142.

Richter, F., Watson, B., Chaussidon, M., Mendybaev, R., Ruscitto, D., 2014. Lithium isotope fractionation by diffusion in minerals. Part 1: pyroxenes. Geochim. Cosmochim. Acta 126, 352–370.

Rubatto, D., 2017. Zircon: The Metamorphic Mineral. Rev. Miner. Geochem, pp. 261–295.
Shamloo, H.I., Till, C.B., Hervig, R.L., 2021. Multi-mode magnesium diffusion in sanidine: applications for geospeedometry in magmatic systems. Geochim. Cosmochim. Acta 298, 55–69.
Shannon, R.D., 1976. Revised effective ionic radii and systematic studies of interatomic distances in halides and chalcogenides. Acta Crystallogr., Sect. A 32, 751–767.
Sinh, V.B.T., Osanai, Y., Lenz, C., Nakano, N., Adachi, T., Belousova, E., Kitano, I., 2019. Gem-quality zircon megacrysts from placer deposits in the central highlands, Vietnam—potential source and links to Cenozoic Alkali Basalts. Minerals 9.
Sliwinski, J.T., Kueter, N., Marxer, F., Ulmer, P., Guillong, M., Bachmann, O., 2018. Controls on lithium concentration and diffusion in zircon. Chem. Geol. 501, 1–11.
Spencer, C.J., Kirkland, C.L., Taylor, R.J.M., 2016. Strategies towards statistically robust interpretations of in situ U–Pb zircon geochronology. Geosci. Front. 7, 581–589.
Stepanov, A.S., Rubatto, D., Hermann, J., Korsakov, A.V., 2016. ContrastingP-Tpaths within the Barchi-Kol UHP terrain (Kokchetav complex): implications for subduction and exhumation of continental crust. Am. Mineral. 101, 788–807.
Suzuki, K., Kouta, H., Nagasawa, H., 1992. Hf-Zr interdiffusion in single crystal zircon. Geochim. J. 26, 99–104.
Tailby, N.D., Walker, A.M., Berry, A.J., Hermann, J., Evans, K.A., Mavrogenes, J.A., O'Neill, H.S.C., Rodina, I.S., Soldatov, A.V., Rubatto, D., Sutton, S.R., 2011. Ti site occupancy in zircon. Geochim. Cosmochim. Acta 75, 905–921.
Tang, M., Rudnick, R.L., McDonough, W.F., Bose, M., Goreva, Y., 2017. Multi-mode Li diffusion in natural zircons: evidence for diffusion in the presence of step-function concentration boundaries. Earth Planet. Sci. Lett. 474, 110–119.
Timms, N.E., Erickson, T.M., Pearce, M.A., Cavosie, A.J., Schmieder, M., Tohver, E., Reddy, S.M., Zanetti, M.R., Nemchin, A.A., Wittmann, A., 2017. A pressure-temperature phase diagram for zircon at extreme conditions. Earth-Sci. Rev. 165, 185–202.
Tompkins, H.G.D., Zieman, L.J., Ibañez-Mejia, M., Tissot, F.L.H., 2020. Zirconium stable isotope analysis of zircon by MC-ICP-MS: methods and application to evaluating intra-crystalline zonation in a zircon megacryst. J. Anal. At. Spectrom. 35, 1167–1186.
Wilde, S.A., Valley, J.W., Peck, W.H., Graham, C.M., 2001. Evidence from detrital zircons for the existence of continental crust and oceans on the Earth 4.4 Gyr ago. Nature 409, 175–178.
Yund, R.A., Snow, E., 1989. Effects of hydrogen fugacity and confining pressure on the interdiffusion rate of NaSi-CaAl in plagioclase. J. Geophys. Res., Solid Earth 94, 10662–10668.